JOURNAL OF MATERIALS SCIENCE 27 (1992) 5357–5364

Mechanical behaviour of SiC fibre-reinforced titanium/titanium aluminide hybrid composites

S. M. JENG, J.-M. YANG
Department of Materials Science and Engineering, University of California, Los Angeles, CA 90024, USA

D. G. ROSENTHAL, S. AKSOY
Textron Lycoming, Stratford, CT 06497, USA

The viability of developing an SiC fibre-reinforced titanium/titanium aluminide hybrid matrix composite was explored. The hybrid composites are expected to be used at temperatures beyond those attainable in conventional titanium matrix composites while improving the damage tolerance of the titanium aluminide matrix composites. The room-temperature mechanical characteristics studied were tensile strength, fracture toughness, low-cycle fatigue life and fatigue crack growth rate. The mechanisms of damage initiation and propagation under various loading conditions were also characterized. The directions for developing a satisfactory composite with hybrid titanium/titanium aluminide matrix are also addressed.

1. Introduction

Advanced metal-matrix composites based upon titanium alloys and titanium–aluminium intermetallic alloys (Ti_3Al, TiAl) reinforced with SiC fibres are the most promising materials for high-temperature structural applications. Potential applications of these novel materials include gas turbine engines, airframes for hypersonic aircraft and advanced energy conversion systems. The disordered titanium alloys have a unique combination of several attractive properties that make them ideal matrix material for a composite. These include higher ductility, lower density compared to steel and nickel-based alloys, a higher strength-to-weight ratio compared to aluminium and steel, and excellent creep and corrosion resistance. Reinforcing titanium alloys with high-stiffness and high-strength ceramic fibres results in significant improvement in specific stiffness and specific strength. However, the service temperature of these alloys has generally been limited to approximately 600 °C. This will limit the service temperature of composites based upon titanium alloy matrices.

Ordered titanium–aluminium intermetallic alloys such as Ti_3Al and TiAl have a number of intrinsic properties that make them more appealing than conventional titanium alloys for high-temperature applications [1]. The higher aluminium content makes the aluminides less dense than disordered titanium alloys, and appreciably less dense than nickel-based superalloys. In addition, the titanium aluminides have better resistance to high-temperature oxidation, better creep resistance, and higher stiffness than conventional titanium alloys. However, the ductility and fracture toughness of the titanium aluminide is lower than that of the conventional titanium alloys, especially at low temperatures. As a result, composites based upon brittle titanium aluminide matrices may suffer from poor impact resistance and damage tolerance. Also, microcracking of the matrix or interfacial region resulting from the thermal expansion mismatch between the fibre and matrix may occur during composite processing and thermal cycling [2, 3]. The microcracking will extend into the matrix upon loading and lead to the premature failure of the composite. In order to improve further the damage tolerance, mechanical and environmental reliability, and elevated-temperature properties to meet the increasingly demanding design requirements, effort has been directed towards developing composites with hybrid matrices. Matrix hybridization has been demonstrated as a viable approach to improve further the performance of metal and intermetallic matrix composites [4, 5].

The objective of this work was to demonstrate the viability of using the combination of a ductile titanium alloy and a brittle titanium aluminide as a composite matrix. The mechanical properties, damage mechanisms and fracture behaviour of SCS-6 fibre-reinforced titanium/titanium aluminide hybrid matrix composites under various loading conditions were characterized. The behaviour of the SCS-6/titanium and SCS-6/titanium aluminide monomatrix composites under various loading conditions can be found in [6–9].

2. Materials and experimental procedures

The material used in this study was unidirectional SCS-6 fibre-reinforced Ti–6 at % Al–4 at % V (Ti–6–4) and Ti–25 at % Al–10 at % Nb–3 at % V–1 at % Mo (Ti–25–10) hybrid composite..The microstructure and laminate lay-up of the composite are shown in Fig. 1.

0022–2461

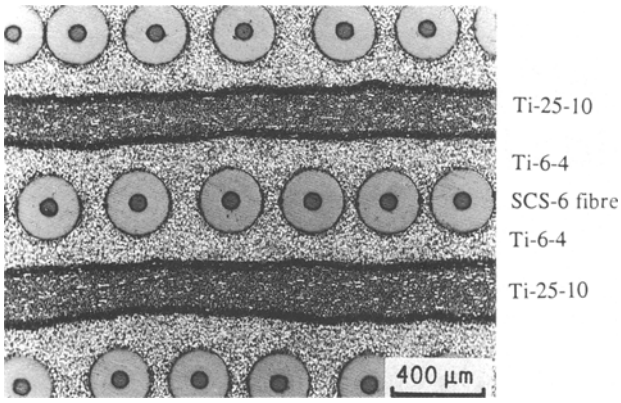

Figure 1 The microstructure and laminate lay-up of the SCS-6/Ti–6–4/Ti–25–10 hybrid composite.

The Ti–25–10 foils were placed between the SCS-6/Ti–6–4 lamina and at the outer layer of the composite. The thicknesses of the SCS-6/Ti–6–4 composite lamina and the Ti–25–10 foils after consolidation were 0.12 and 0.26 mm, respectively. The volume fraction of the fibre, Ti–6–4 and Ti–25–10 were 0.2, 0.45 and 0.35, respectively. The composite plate (150 mm × 100 mm × 2 mm) with five layers of the SCS-6/Ti–6–4 and six layers of Ti–25–10 was consolidated by a vacuum diffusion bonding technique. Parts of the as-fabricated composite panel and the matrix alloy were isothermally exposed at 800 °C in vacuum for 50 and 100 h.

Tensile tests were conducted on the composite in the as-fabricated state and isothermally exposed conditions. Specimens having dimensions of 100 mm × 6.25 mm were machined from each panel with fibres parallel to the length direction. Thin-foil strain gauges were mounted on both sides of the specimen to measure the strain-to-failure. Titanium alloy tabs were epoxy bonded to both sides of the specimen ends to protect the grip section during testing. The tensile test was conducted at room temperature on an Instron testing machine operated at a crosshead speed of 0.5 mm min^{-1}.

Three-point bending tests on chevron-notched specimens were conducted to evaluate the toughness of the composite in the as-fabricated and isothermally exposed conditions. Specimens were mounted in a three-point-bending fixture with a span length of 50 mm and loaded to failure on an Instron machine at a crosshead speed of 0.5 mm min^{-1}. Upon loading, a crack initiated and propagated in a well-controlled manner until complete fracture of the specimen. The critical load, P_c, was identified by a discontinuity in the load–deflection curve. The energy under the load–deflection curve up to the critical load was considered to be the critical energy to initiate the crack, W_i. The normalized energy to crack initiation was calculated as $\gamma_i = W_i/t$, where t is the specimen thickness. The area under the load–deflection curve is considered to be equal to the total energy absorbed during the whole fracture process, W_F. The work-of-fracture, γ_f, was computed as $\gamma_f = W_F/2A$, where A is the area of the fracture surface.

Low-cycle fatigue tests were conducted on unnotched specimens to determine the number of cycles to failure as a function of cyclic stress level. The specimens had dimensions of 76 mm × 6.5 mm. The specimen edges were polished to remove a 5–10 μm of surface damage layer. The testing was conducted on a close-loop servo-hydraulic Instron testing machine with a maximum capacity of 100 kN at $f = 10$ Hz, $R = 0.1$, in a load-controlled sine-wave mode. The applied maximum cyclic stresses varied from 0.3–0.8 of the composite tensile strength. Fatigue crack propagation rate was measured using specimens with a chevron notch. The notch was perpendicular to the fibre direction. The specimen had dimensions of 76 mm × 12.5 mm. The maximum applied cyclic stresses were 150 and 195 MPa. The testing was conducted in a load-controlled mode with $f = 20$ Hz and $R = 0.1$. The applied stress intensity factors, ΔK, were calculated using

$$\Delta K = YW^{1/2}(\sigma_{max} - \sigma_{min}) \quad (1)$$

with

$$Y = 1.99\,(a/W)^{1/2} - 0.41\,(a/W)^{3/2} + 18.7\,(a/W)^{5/2} - 38.48\,(a/W)^{7/2} + 53.85\,(a/W)^{9/2} \quad (2)$$

where W is the specimen width, a the crack length, σ_{max} and σ_{min} the maximum and minimum stress level. The crack length after a pre-determined number of cycles was periodically measured using an optical microscope.

Fractographic analysis was performed on all test specimens using a scanning electron microscope. Selected sections of the specimen after testing were metallographically polished and examined by an optical microscope. The mechanisms of crack initiation and propagation under various loading conditions were determined.

3. Results and discussion

3.1. Tensile behaviour

The typical stress–strain curves of the SCS-6/Ti–6–4/Ti–25–10 hybrid composite in the as-fabricated and isothermally exposed at 800 °C states are shown in Fig. 2. The composite exhibited a nonlinear stress–strain response in both the as-fabricated and isothermally exposed states. The linear to nonlinear transition of the stress–strain curve occurred at a strain level of 0.3% in the as-fabricated composite. However, after thermal exposure, the transition occurred at a higher strain level (0.45%). The elastic modulus, and ultimate tensile strength of the composites are listed in Table I. The results indicate that extended thermal exposure at 800 °C results in a slight decrease in elastic modulus. However, the tensile strength increased slightly after exposure at 800 °C for 50 and 100 h.

Fig. 3 shows the tensile fracture surface of the SCS-6/Ti–6–4/Ti–25–10 hybrid composite in the as-fabricated state. Brittle fracture with minimum fibre pull-out was observed throughout the fracture surface of the composite. However, ductile fracture with dimpling was observed in the Ti–6–4 matrix. Fibre/matrix debonding was also observed at the fracture

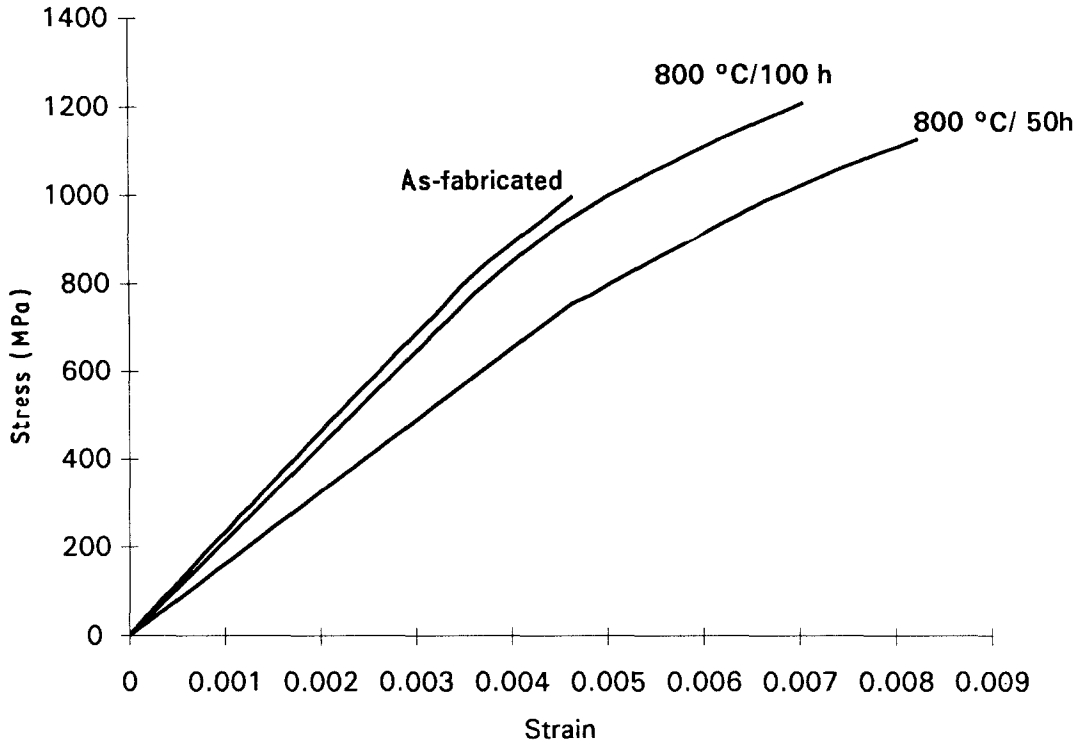

Figure 2 The typical stress–strain curves of the SCS-6/Ti–6–4/Ti–25–10 hybrid composite.

TABLE I Mechanical properties of the SCS-6/Ti–6–4/Ti–25–10 composite

Condition	Young's modulus (GPa)	Ultimate tensile strength (MPa)	Normalized crack initiation energy, γ_i ($J\,m^{-1}$)	Work-of-fracture, γ_f ($kJ\,m^{-2}$)
As-fabricated	210 ± 23	1138 ± 20	157 ± 20	24.6 ± 2.7
800 °C/50 h	165 ± 2	1166 ± 44	93 ± 3	13.9 ± 2.2
800 °C/100 h	210 ± 12	1193 ± 31	92 ± 7	15.3 ± 3.5

surface as shown in Fig. 3b. Interfacial debonding was found along the interfacial reaction layer and the outer carbon-rich layer. Delamination was also observed along the diffusion bonding interface. Fig. 3c shows the optical micrographs of the polished surface parallel to the tensile surface. Multiple fibre fracture and matrix plastic failure near the fracture surface can be observed. A close examination of the polished surface also indicates that microcracks initiated at the fibre/matrix interface as shown in Fig. 4. However, the propagation of the microcrack was inhibited due to the microyielding of the Ti–6–4 matrix and the presence of a carbon-rich layer on the fibre surface. A previous study on the SCS-6/Ti–25–10 composite indicated that the crack initiated from the brittle interfacial reaction layer would propagate into the matrix. This will lead to catastrophic failure of the composite [7]. The above results imply that the formation of matrix cracks can be suppressed by using the hybrid approach. The interface between the Ti–6–4 and Ti–25–10 matrix remained well-bonded as shown in Fig. 5.

The tensile fracture surface of the composite after exposure at 800 °C is shown in Fig. 6. There is no apparent difference in fracture morphology between the as-fabricated and heat-treated specimens. However, delamination along the diffusion-bonded interface was not observed in the thermally exposed specimens. This might be due to the recrystallization of the matrix along the diffusion-bonded interface. Furthermore, after thermal exposure, a significant amount of microcracking was observed near the interface between Ti–6–4 and Ti–25–10 alloys as shown in Fig. 7. The microcracking was also found in the Ti–25–10 matrix.

3.2. Work of fracture

The typical load–deflection curves obtained during the work of fracture test of the SCS-6/Ti–6–4/Ti–25–10 hybrid composite in the as-fabricated and isothermally exposed states are shown in Fig. 8. The SCS-6/Ti–6–4/Ti–25–10 hybrid composite exhibited a noncatastrophic failure behaviour in both the as-fabricated and isothermally exposed states. The normalized crack initiation energy and work of fracture calculated from these curves are also listed in Table I. The crack initiation energy and work of fracture of the composite decreased slightly after exposure.

Fig. 9 shows the crack propagation pattern of the as-fabricated SCS-6/Ti–6–4/Ti–25–10 hybrid composite during the work of fracture test. The crack did not exhibit a planar propagation behaviour. As shown in the micrograph, the crack was initially deflected at

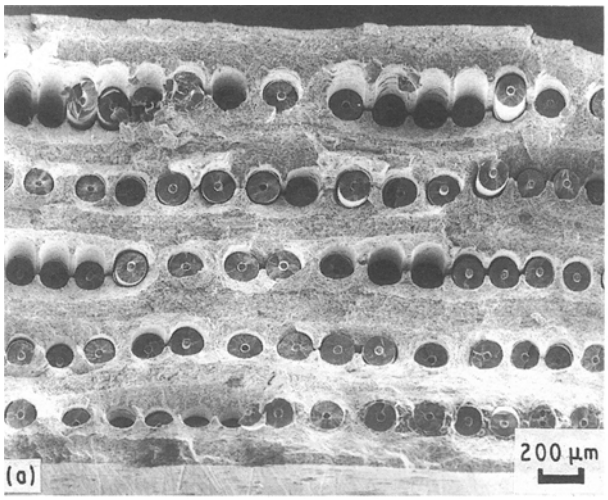

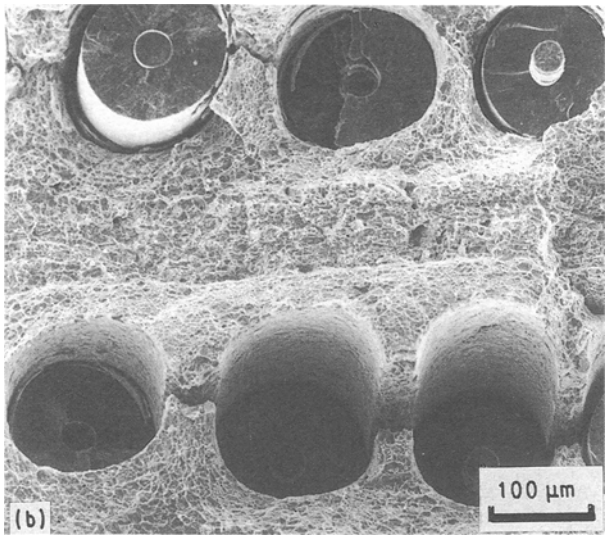

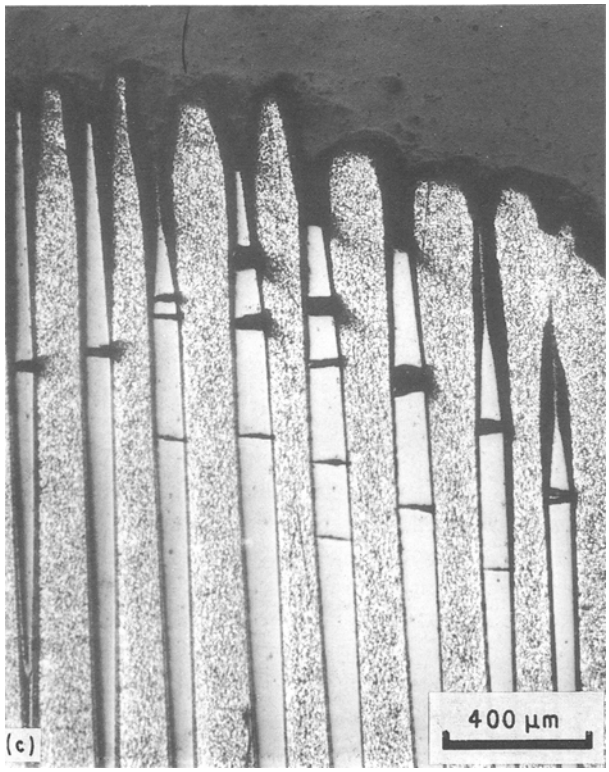

Figure 3 (a, b) Tensile fracture surface, and (c) polished surface of the as-fabricated SCS-6/Ti–6–4/Ti–25–10 hybrid composite.

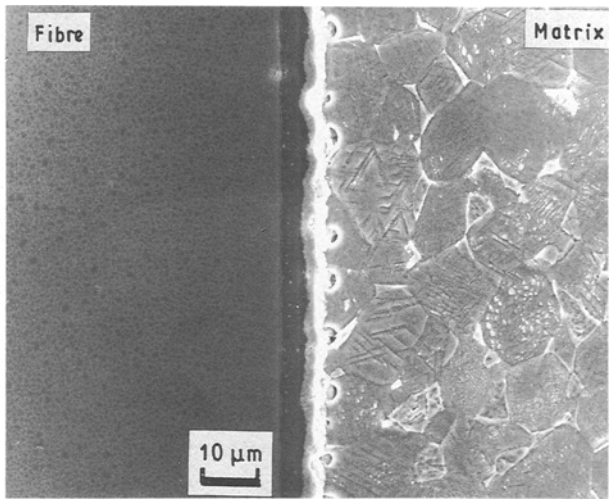

Figure 4 Interfacial cracking after tensile testing in SCS-6/Ti–6–4/Ti–25–10 hybrid composite.

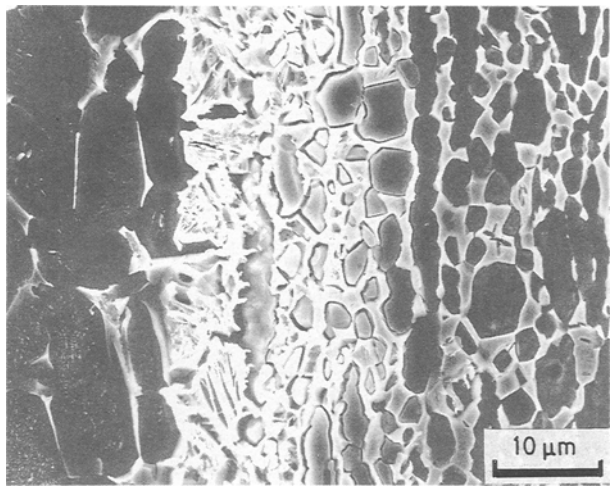

Figure 5 The interfacial region between two matrix alloys in the as-fabricated SCS-6/Ti–6–4/Ti–25–10 hybrid composite after tensile testing.

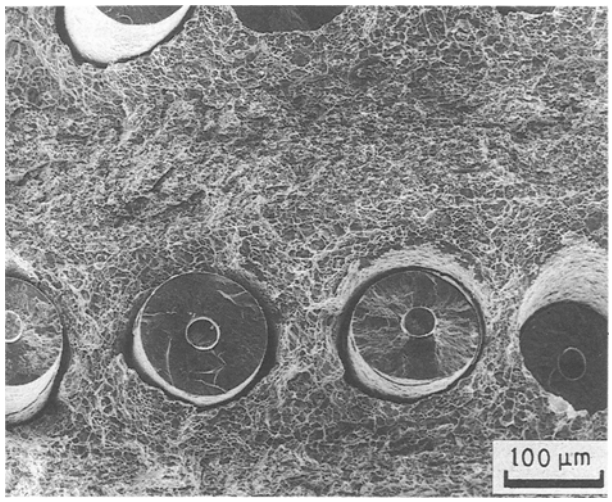

Figure 6 The tensile fracture surface of the SCS-6/Ti–6–4/Ti–25–10 composite after isothermal exposure.

angle of approximately 45° to the notch plane. Fibre fracture and plastic deformation in the Ti–6–4 matrix was clearly observed along the crack path. Several micro-failure mechanisms were found in the crack-tip damage zone including multiple fibre fracture, matrix

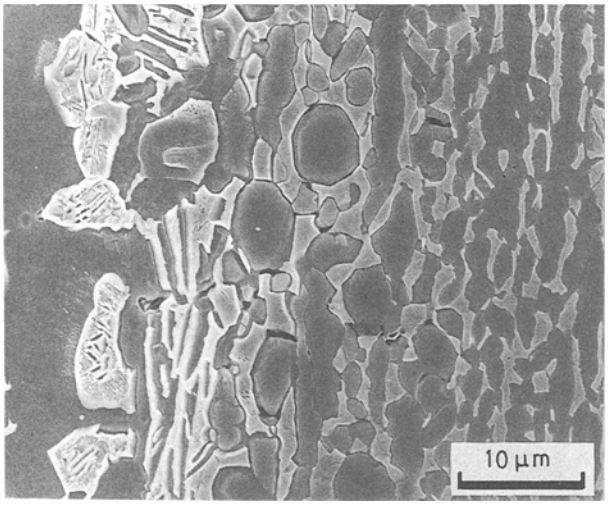

Figure 7 The interfacial region between two matrix alloys in the heat-treated SCS-6/Ti–6–4/Ti–25–10 composite after tensile testing.

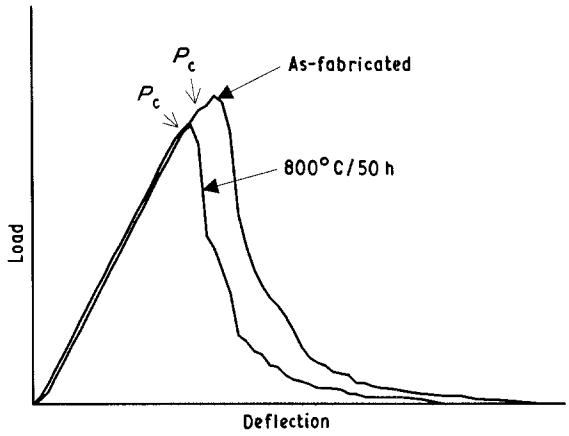

Figure 8 Load–deflection curves of the SCS-6/Ti–6–4/Ti–25–10 hybrid composite after the three-point bending test.

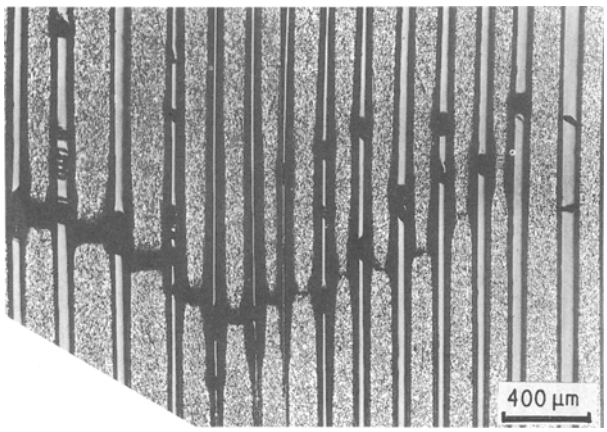

Figure 9 Crack propagation pattern of the SCS-6/Ti–6–4/Ti–25–10 hybrid composite.

plastic deformation and fibre/matrix interfacial debonding. The plastic deformation of the ductile titanium layer would enhance the energy absorbing capability of the hybrid composites. Further examination of the polished surface revealed that the crack propagation patterns in the Ti–6–4 and Ti–25–10 layer were different. In the Ti–25–10 matrix, significant crack branching and secondary cracking was observed as shown in Fig. 10a. However, in the Ti–6–4 matrix, only one dominant crack was found as shown in Fig. 10b. The crack propagating behaviour and failure mechanisms of the composite after thermal exposure is similar to that of composite in the as-fabricated state.

3.3. Low-cycle fatigue behaviour

The maximum applied cyclic stress versus the number of cycles to failure (S–N curve) of the as-fabricated SCS-6/Ti–6–4/Ti–25–10 composite is plotted in Fig. 11. The composite exhibited a linear relationship between the applied stress and the number of cycles to failure at applied stresses below 80% of its tensile

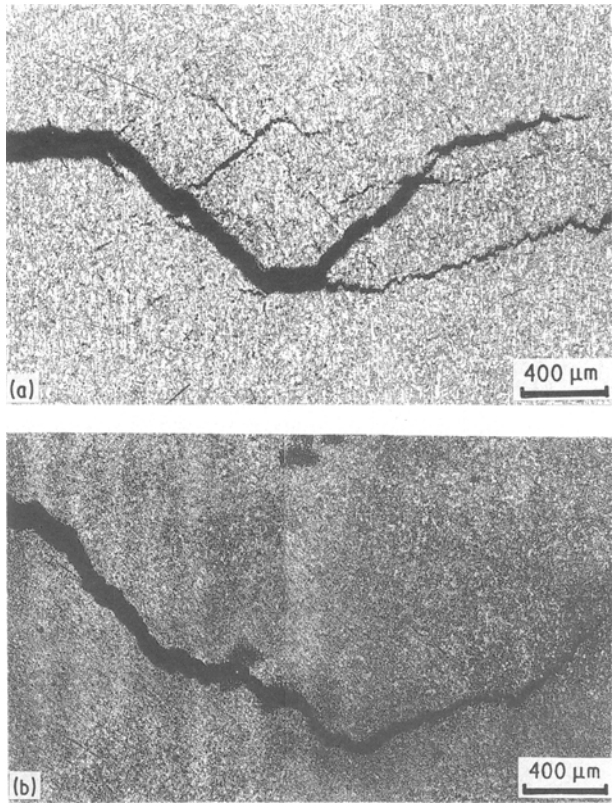

Figure 10 (a, b) Crack propagation pattern in Ti–25–10 and Ti–6–4 matrices.

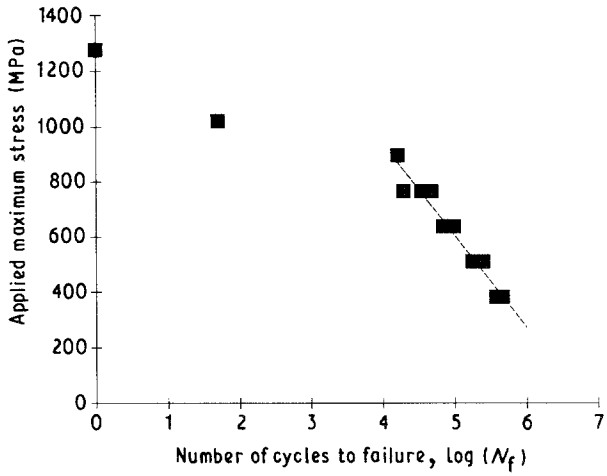

Figure 11 The fatigue life of the SCS-6/Ti–6–4/Ti–25–10 hybrid composite.

strength. In addition, the composite did not show a clear fatigue limit in these stress ranges.

Fig. 12 shows the fatigue damage modes of the hybrid composite. Fig. 12a shows a typical fatigue fracture surface of the hybrid composite. The composite exhibited a flat fracture surface without significant fibre pull-out. The figure indicates that the fatigue crack initiated at the interfacial reaction layer at the specimen edge. Fig. 12b is the micrograph showing the fatigue damage along the plane perpendicular to the laminate. It clearly shows that the crack propagated directly into both matrices without being deflected along the interface between the Ti–6–4 and Ti–25–10 matrix alloys. However, in the SCS-6/Ti–6–4 region, the crack was deflected along the fibre/Ti–6–4 interface and caused fibre failure and matrix cracking. Fig. 12c shows the damage modes in the SCS-6/Ti–6–4 lamina. The crack propagated perpendicular to the fibre direction. A significant amount of fibre fracture occurred above and below the crack plane. However, at the fatigue crack-tip region, it was found that the crack was bridged by unbroken fibres. This suggests that matrix cracking occurred prior to fibre fracture. Furthermore, multiple matrix cracking that occurred in the SCS-6/Ti alloy monomatrix composite was not observed in the hybrid composite. This may be due to the lower fibre volume fraction in the hybrid composite than that in the SCS-6/Ti alloy monomatrix composites used in a previous study (> 35%) [6–9]. The fibres could not carry the extra load released from the cracked matrix and fractured in the wake of the crack.

3.4. Fatigue crack propagation

The fatigue cracking length versus the number of cycles at applied stresses of 150 and 195 MPa is plotted in Fig. 13. The applied ΔK values are also listed in this figure. For the applied maximum stress at 150 MPa (initial $\Delta K_i = 17\ \text{MPa m}^{1/2}$), the crack growth rate decreased and approached a constant value after 10^5 cycles. However, for the applied stress at 195 MPa ($\Delta K_i = 34\ \text{MPa m}^{1/2}$), the crack growth rate was almost constant throughout the whole crack propagation process. The results indicate that the fatigue crack growth behaviour is different from that of the matrix alloy. The crack growth rate increases as the crack advances. The constant fatigue crack growth rates were calculated to be 7×10^{-7} and 3.3×10^{-6} mm/cycle for applied stresses at 150 and 195 MPa, respectively. The fatigue crack growth rates of the hybrid composite are two to three orders of magnitude lower than that of Ti–25–10 and Ti–6–4 matrix alloys [10, 11].

Microstructural examination indicated that the fatigue crack propagated along the original notch plane as shown in Fig. 14. Crack deflection and branching were not observed. Fibre pull-out in the wake of the fatigue crack was also observed. The fibre pull-out lengths were measured to be between 40 and 180 μm. Fig. 15 is a scanning electron micrograph of the fatigue crack tip region. Fibre fracture and interfacial debonding along the fibre/matrix was observed in front of the fatigue crack tip. The local stress distribution in front of a fatigue crack tip has been calculated by Chan [12]. The result indicated that the maximum stress normal to the fibre/matrix interface occurred directly ahead of the crack tip. This localized stress concentration will cause interfacial debonding. From the above microstructural observation, it is believed that crack tip interfacial debonding and fibre pull-out in the wake of the crack were the major factors responsible for the fatigue crack growth behaviour in the hybrid composite. The interfacial debonding will blunt the crack tip and reduce the effective driving

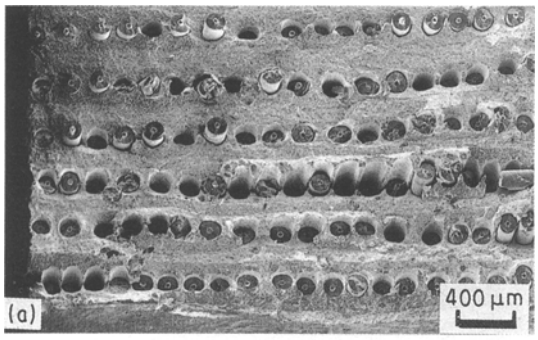

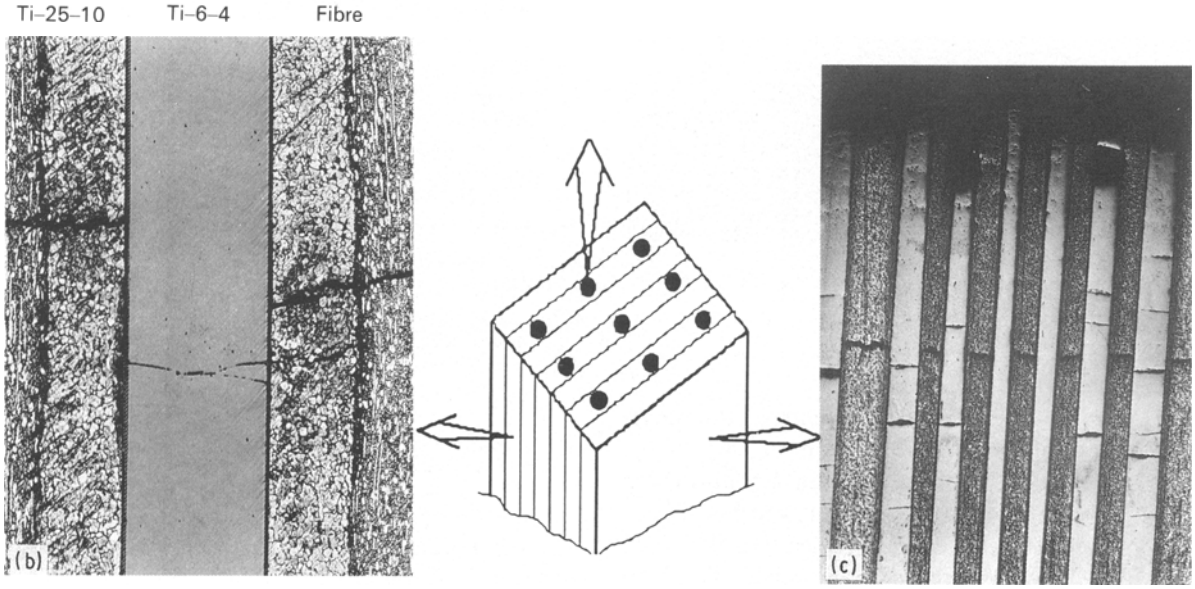

Figure 12 (a–c) The fatigue damage in the SCS-6/Ti–6–4/Ti–25–10 hybrid composite.

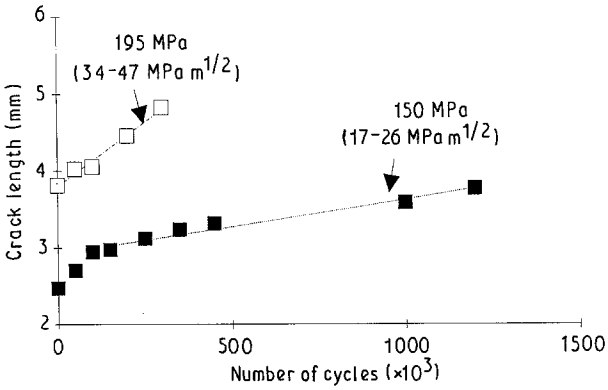

Figure 13 The fatigue crack length versus number of cycles of the SCS-6/Ti–6–4/Ti–25–10 hybrid composite.

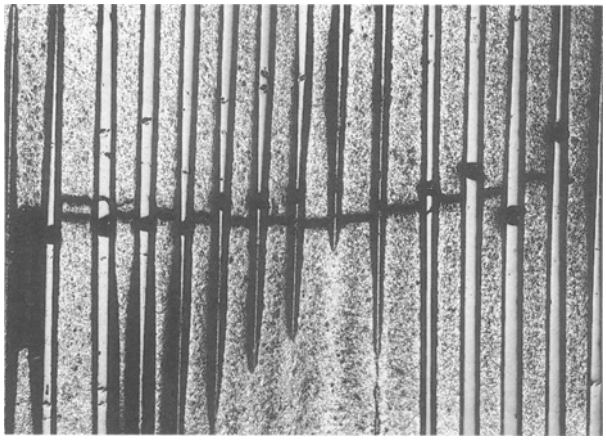

Figure 14 The fatigue crack propagation pattern of the SCS-6/Ti–6–4/Ti–25–10 hybrid composite.

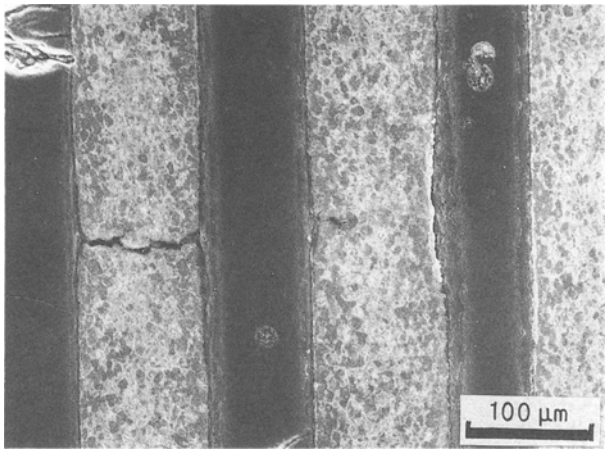

Figure 15 The fatigue crack tip damage zone of the SCS-6/Ti–6–4/Ti–25–10 hybrid composite.

force (ΔK). Furthermore, the frictional stress induced by the fibre pull-out process will reduce the applied σ_{max} and increase σ_{min} at the fatigue crack tip. This, in turn, will reduce the applied ΔK. A detailed analysis of crack tip blunting and fibre pull-out sliding mechanisms on the fatigue crack growth of the fibre-reinforced metal-matrix composite is being conducted.

4. Conclusion

A composite based upon the ductile titanium alloy and brittle titanium aluminide hybrid matrix reinforced with SCS-6 fibres has been successfully fabricated. The SiC fibres are surrounded by the ductile titanium alloy. This ductile layer can serve as a compliant layer to accommodate the residual stresses. Furthermore, it can effectively suppress the propagation of microcracks initiated from the brittle interfacial reaction layer. The titanium aluminide layers provide better high-temperature properties and environmental resistance. The resulting composite can be used at temperatures beyond those attainable in titanium alloy matrix composites while improving the damage tolerance of the titanium aluminide matrix composites. The results obtained from this study clearly indicate that composites with hybrid matrices have a combination of several unique attractive properties. However, more work is needed to explore further the potential of using hybrid titanium/titanium aluminide matrix composites for structural applications.

The mechanical behaviour of a composite with hybrid matrix depends on several factors such as fibre volume fraction, fibre type and the relative amount of titanium/titanium aluminide and laminate stacking sequence. The combination of Ti–6Al–4V ($\alpha + \beta$ alloy) and Ti–25Al–10Nb–3V–1Mo ($\alpha_2 + \beta$ alloy) was selected as a model system to demonstrate the viability of the hybrid approach. However, several other combinations of titanium alloys can also be used as composite matrices. This includes the combination of metastable β alloy (such as Ti–15V–3Al–3Cr–3Sn) or stable β alloy (such as Ti-1100) with titanium aluminide. Certainly, the type of alloy used will affect the processability, residual stress, mechanical behaviour and service temperatures of the resulting composites. In addition, the relative amount of titanium/titanium aluminide will also affect the fibre content, mechanical behaviour and deformation characteristics of the composite. Therefore, the hybrid approach has opened up a significant opportunity for tailoring a new family of structural materials with desired mechanical properties.

Acknowledgements

This work was partially supported by the National Science Foundation through the Presidential Young Investigator Award to J.-M. Yang (MSS 9057030). The authors thank Mr Tu-Hoan Bruce Nguyen for reviewing the manuscript.

References

1. H. A. LIPSITT, in "High-Temperature Ordered Intermetallic Alloys I", Vol. 39, edited by C. C. Koch, C. T. Liu and N. S. Stoloff (Materials Research Society, 1985) p. 351.
2. J.-M. YANG and S. M. JENG, *Scripta Metall.* **23** (1989) 1559.

3. P. K. BRINDLEY, P. A. BARTOLOTTA and R. A. MACKAY, HITEMP Review: Advanced High Temperature Engine Materials Technology Program, NASA CP-10039 (1989) p. 14.
4. M. S. MADHUKAR, A. FAREED, J. AWERBUCH and M. J. KACZAK, in "High Temperature/High Performance Composites", Vol. 120, edited by F. D. Lemkey, S. G. Fishman, A. G. Evans and J. R. Strife (Materials Research Society, Pittsburgh, 1988) p. 121–8.
5. J. J. PETROVIC and R. E. HONNELL, *Ceram. Engng Sci. Proc.* **11** (1990) 734.
6. J.-M. YANG, S. M. JENG and C. J. YANG, *Mater. Sci. Engng* **A138** (1991) 155.
7. S. M. JENG, C. J. YANG and J.-M. YANG, *ibid.* **A138** (1991) 169.
8. *Idem, ibid.* **A138** (1991) 181.
9. S. M. JENG, P. ALASSOEUR, J.-M. YANG and S. ALSOY, *ibid.* **A148** (1991) 67.
10. K. S. CHAN and D. L. DAVIDSON, *Metall. Trans.* **12A** (1990) 1603.
11. P. B. ASWATH and S. SURESH, *ibid.* **22A** (1991) 817.
12. K. S. CHAN, *Fatigue Fract. Engng Mater. Struct.* **13** (1990) 171.

Received 17 June
and accepted 16 December 1991